DRFC/CAD EUR-CEA-FC-1478

ON SELF-CONSISTENT RAY-TRACING AND FOKKER-PLANCK MODELING OF THE HARD X-RAY EMISSION DURING LOWER-HYBRID CURRENT DRIVE IN TOKAMAKS

J. P. Bizarro, Y. Peysson, P. T. Bonoli, J. Carrasco, T. Dudok de Wit, V. Fuchs, G. T. Hoang, X. Litaudon, D. Moreau, C. Pocheau, and I. P. Shkarofsky

Avril 1993

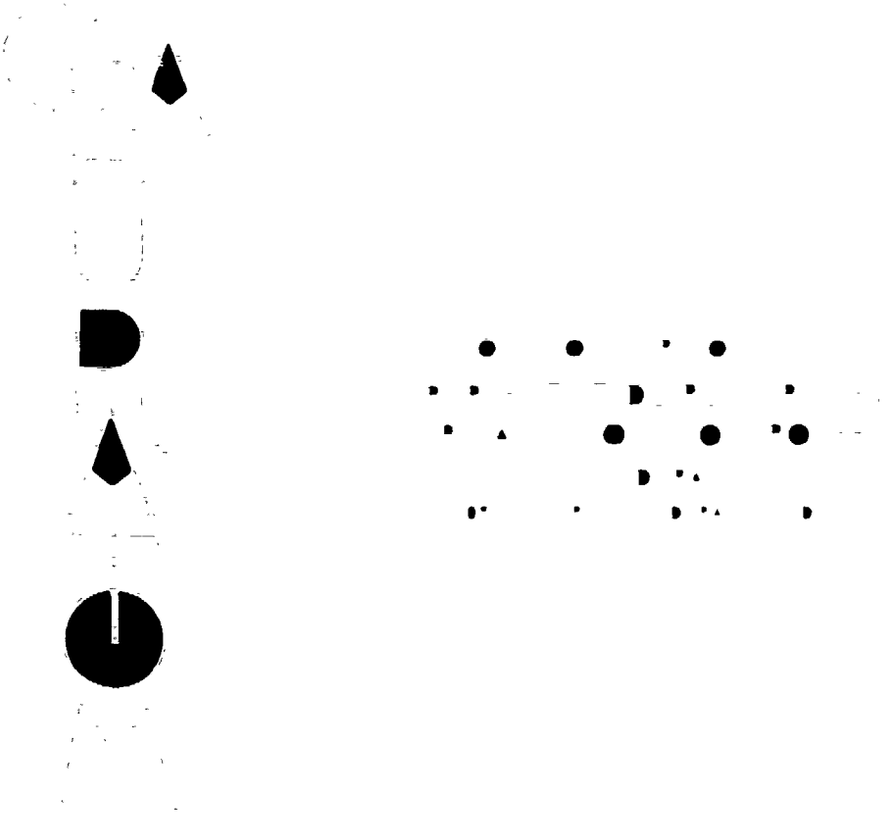

On self-consistent ray-tracing and Fokker-Planck modeling of the hard x-ray emission during lower-hybrid current drive in tokamaks

João P. Bizarro[a)], Yves Peysson, Paul T. Bonoli[b)], Joël Carrasco, Thierry Dudok de Wit, Vladimir Fuchs[c)], Gia T. Hoang, Xavier Litaudon, Didier Moreau, Christine Pocheau, and Issie P. Shkarofsky[d)]

Département de Recherches sur la Fusion Contrôlée, Association Euratom-CEA,

Centre d'Etudes de Cadarache, 13108 St. Paul lez Durance Cedex, France

ABSTRACT

A detailed investigation is presented on the ability of combined ray-tracing and Fokker-Planck calculations to predict the hard x-ray (HXR) emission during lower-hybrid (LH) current drive in tokamaks when toroidally induced ray stochasticity is important. A large number of rays is used and the electron distribution function is obtained by self-consistently iterating the appropriate LH power deposition and Fokker-Planck calculations. Most of the experimentally observed features of the HXR emission are correctly predicted. It is found that corrections due to radial diffusion of suprathermal electrons and to radiation scattering by the inner wall can be significant.

PACS numbers: 52.70.La, 52.50.Gj, 42.20.Cc, 52.65.+z.

I. INTRODUCTION

Combined ray-tracing and Fokker-Planck calculations[1-3] have been shown[4,5] to be successful in modeling lower-hybrid (LH) current drive experiments in tokamaks when toroidally induced ray stochasticity[6,7] is important. Although the validity of geometrical optics can be questioned when stochastic effects prevail, it has been suggested[4,5] that, if a sufficiently large number of rays is used, ray tracing still accurately and reliably describes the dynamics of the launched power spectrum. Ray tracing may then be regarded as an effective Monte Carlo-like method of diffusing the LH energy density in the wave phase space. In particular, the steady-state values and time responses of parameters that depend on the characteristics of the suprathermal electron population created by the LH wave, like the loop voltage and the internal inductance, have been well simulated[4]. These results indicate that the models involved are consistent with the experimental phenomenology.

However, a more stringent test on the validity of such models is still possible, and that is to see how well they reproduce the features of the hard x-ray (HXR) emission observed during LH current drive, which are intimately related to the distribution of suprathermal electrons in configuration and momentum spaces[8-14]. Comparison between theory and experiment has proceeded essentially by adjusting free parameters in a model electron distribution function, such as the "three-temperature distribution", in order to obtain a good fit to the measured HXR data[8-12,14]. Notwithstanding some good results, this method is somewhat unsatisfactory, since the electron distribution function it uses does not have the typical LH-generated plateau resulting from a self-consistent calculation coupling the LH wave propagation and absorption with an appropriate Fokker-Planck analysis of the electron dynamics[1,2]. This self-consistency is naturally incorporated in combined ray-tracing and Fokker-Planck codes, which account for the quasilinear modifications induced by the LH wave in the electron distribution function, as they iterate the LH power deposition and the Fokker-Planck calculations[1-3]. It is the purpose of the present work to provide a detailed investigation on the ability of these codes to predict the HXR emission during LH current drive.

This article is organized as follows: model and experiment details are described in Sec. II, results are presented and discussed in Sec. III, and are summarized in Sec. IV.

II. MODEL AND EXPERIMENT DETAILS

A. Simulation code and benchmarking parameters

To carry out the proposed study, a well-known and documented simulation code[1-5] has been used. It couples three distinct modules: a one-dimensional radial transport module that evolves the thermal plasma[2], a multiple-pass toroidal ray-tracing and power deposition module[1,2], and a one-dimensional (in parallel momentum) Fokker-Planck module[1,2]. In the Fokker-Planck calculation, which is self-consistently iterated with the power deposition calculation[1-3], the suprathermal electron distribution function is assumed to be Maxwellian in perpendicular momentum, with an effective perpendicular temperature that is estimated according to theory[15] in the nonrelativistic limit. Corrections due to trapped particles[16] are incorporated. The code also includes feedback stabilization of the plasma current and radial diffusion of the LH-driven current density[3]. Accurate representations of the poloidal extent of the antenna and of its radiated power spectrum are used[4], thus ensuring that the initial conditions for the ray-tracing calculation correctly reproduce the injected LH power distribution both in poloidal angle and in parallel wave index, $n_{//}$.

This code has been experimentally benchmarked[4], and the analysis performed below has been carried out for the combined Ohmic-LH steady state of TORE SUPRA shot #5319. The basic plasma characteristics are: helium gas ($Z_{He} = 2$), major radius $R_0 = 2.34$ m, minor radius $a = 0.78$ m, magnetic field on axis $B_0 = 3.9$ T, plasma current $I_P = 1.6$ MA, central electron density $n_{e0} \approx 5.3 \times 10^{19}$ m^{-3}, volume-averaged electron density $\langle n_e \rangle \approx 3.3 \times 10^{19}$ m^{-3}, central electron temperature $T_{e0} \approx 3.1$ keV, volume-averaged electron temperature $\langle T_e \rangle \approx 1.5$ keV, and ion effective charge $Z_{eff} \approx 2.8$. The wave frequency is $\omega/2\pi = 3.7$ GHz, and the two main lobes of the launched power spectrum are peaked at $n_{//} = -5.62$ and $n_{//} = 1.59$. The total injected LH power is $P_{in} = 2.46$ MW, 68% of which is launched with $n_{//} > 0$. The power P_{in} is equally

divided into the four poloidal locations corresponding to the four rows of waveguides that form the LH antenna, which is installed in the low-field side of the equatorial mid-plane and whose poloidal extent is approximately 0.38 radians. The same power spectrum is launched from each of those poloidal locations. The lobes with $n_{//} < 0$ and $n_{//} > 0$ are described using 21 and 100 rays, respectively, which makes a total of 84 rays traced with $n_{//} < 0$ and 400 rays traced with $n_{//} > 0$.

For the given plasma and power spectrum parameters, the dynamics of the lobe with $n_{//} > 0$ is dominated by stochastic effects. As a consequence, significant power deposition is predicted for $\rho \leq 0.5$, together with a noninductive current $I_{LH} = 0.31$ MA, even if the inner half of the plasma is initially poorly accessible[7] to that lobe. Here, ρ designates the normalized radial flux surface coordinate, with $\rho = 1$ at the plasma minor radius. Further details of the simulation code and of the benchmarking can be found in the literature[1-5].

B. Diagnostic set-up

The HXR diagnostic installed in TORE SUPRA[13], which is depicted in Fig. 1, has been designed to study the x-ray photon emission, in the range 30 keV $\leq h\nu \leq$ 700 keV, during LH current drive experiments. Here, h is the Planck constant and ν the radiation frequency. The experimental set-up consists of a multi-channel spectrometer that probes the plasma in a poloidal cross section along five lines-of-sight, which are labelled A, B, C, D, E, and which intersect the equatorial mid-plane at $(R-R_0)/a \approx +0.20, 0.00, -0.33, -0.52, -0.71$, respectively, where R is the distance from the tokamak axis. Lines-of-sight D and E intersect the inner wall, which is covered by 1 cm thick graphite tiles, whereas the three others face an upper port. The collimators are made out of lead and allow different apertures to be selected, in order to adjust the spatial resolution (2 cm to 15 cm). Each detector views the plasma through two circular apertures whose radii are r_1 and r_2, and which are separated by a distance b ($r_1 = 3.5$ mm, $r_2 = 6$ mm, and $b \approx 1.4$ m for TORE SUPRA shot #5319). To prevent signal contamination by the noncollimated HXR emission, all detectors are placed inside a lead box with 10 cm thick walls.

Bismuth germanate, $Bi_4Ge_3O_{12}$ (BGO), scintillators have been chosen[13] due to their high stopping efficiency. Interactions with neutrons and secondary γ rays produced in the detectors vicinity are expected to be significantly reduced, without a large degradation of the photofraction in the energy range of interest. With 23 mm thick BGO crystals, only 10% to 15% of the plasma x-ray emission is lost in the interval $30\ keV \leq h\nu \leq 400\ keV$. Attenuation along the lines-of-sight is kept to a small level above 30 keV by using a 1 mm thick aluminium vacuum window. The BGO luminescence properties under HXR excitation are characterized by a very small afterglow (0.005% after 3 msec), thus enabling a high counting rate (greater than 100 kHz). As compared to standard NaI(Tl) scintillators[8,9,11,12], BGO has a smaller scintillation conversion efficiency and, therefore, a lower energy resolution. However, this does not represent a serious disadvantage, because HXR spectra are always very broad.

C. Prediction of the HXR spectra

The HXR spectrometer is a transducer that transforms the energies $h\nu$ of photons emitted by the plasma into pulses of height H. For a given line-of-sight, and if N_H and $N_{h\nu}$ designate the number of pulses with height H and the number of photons with energy $h\nu$, respectively, the pulse spectrum, $dN_H/dtdh\nu$, and the photon spectrum, $dN_{h\nu}/dtdh\nu$, are linked by the relation

$$\frac{dN_H}{dtdh\nu} = \int_0^\infty dh\nu' \lambda_a(h\nu')\left[1 - \lambda_d(h\nu')\right] g_d(h\nu', H) \frac{dN_{h\nu'}}{dtdh\nu'} . \qquad (1)$$

Here, for a given energy $h\nu$, $\lambda_a(h\nu)$ is an attenuation coefficient representing the fraction of the radiation collected along the line-of-sight that is transmitted up to the detector, $\lambda_d(h\nu)$ the detector transmission coefficient measuring the fraction of the radiation arriving at the detector that does not interact with it, and $g_d(h\nu, H)$ the detector response function (normalized to unity) giving the conversion law between photon energies and pulse heights. Let φ be the angle between the line-of-sight and the toroidal magnetic field. Then, the photon spectrum can be written as[17]

$$\frac{dN_{h\nu}}{dtdh\nu} \cong \left(\frac{\pi r_1 r_2}{b}\right)^2 \int_L dl \frac{dn_{h\nu}(\rho,\varphi)}{d\Omega dtdh\nu}, \tag{2}$$

where dl is the length element along the line-of-sight and L its total length inside the plasma, and $dn_{h\nu}(\rho,\varphi)/d\Omega dtdh\nu$ the density of photons at ρ that are emitted with energy $h\nu$ in the direction φ, per solid angle $d\Omega$, time interval dt, and energy range $dh\nu$.

The main sources of x-ray photons in the range $30\,keV \leq h\nu \leq 700\,keV$ are, in a plasma where a significant suprathermal electron population is present, electron-electron and electron-ion bremsstrahlung radiation[9]. For the plasma of interest here ($Z_{eff} \approx 2.8$), the electron-electron contribution is less than 10% of the total HXR emission[9] and is therefore neglected. Furthermore, fully stripped carbon ($Z_C = 6$) is considered to be the only relevant impurity. Under these conditions, the relativistic Born approximation corrected by the Elwert factor can be used for the electron-ion cross section[9], differential in solid angle and in energy, $d\sigma^{BE}_{e\text{-}i}(h\nu,p,\vec{e_\nu}.\vec{e_p},Z_i)/d\Omega dh\nu$, with Z_i the ion charge, p the momentum of the emitting electron, $\vec{e_p}$ the unitary vector in the direction of the emitting electron, and $\vec{e_\nu}$ the unitary vector in the direction of the emitted photon. Using spherical coordinates to locate the emitting electron in a reference frame such that the local toroidal magnetic field is along the z-axis and the line-of-sight lies in the xz-plane, the following relation applies:

$$\vec{e_\nu}.\vec{e_p} = \cos\theta\cos\varphi + \cos\phi\sin\theta\sin\varphi\,. \tag{3}$$

Then, making $\mu = \cos\theta$, $dn_{h\nu}(\rho,\varphi)/d\Omega dtdh\nu$ reads

$$\frac{dn_{h\nu}(\rho,\varphi)}{d\Omega dtdh\nu} \cong \sum_{i=He,C} n_i(\rho) \int_0^{2\pi} d\phi \int_{-1}^{+1} d\mu \int_{p_{min}}^{\infty} dp$$

$$\times \frac{d\sigma^{BE}_{e\text{-}i}(h\nu,p,\vec{e_\nu}.\vec{e_p},Z_i)}{d\Omega dh\nu} \frac{p^3 c}{(p^2 + m_e^2c^2)^{1/2}} f_{st}(\rho,\mu,p)\,, \tag{4}$$

with $n_i(\rho)$ the ion density, $f_{st}(\rho,\mu,p)$ the suprathermal electron distribution function, m_e the electron mass, c the speed of light, and $p_{min} = (1/c)\left[h\nu\left(h\nu + 2m_ec^2\right)\right]^{1/2}$. In writing Eq. (4), the poloidal and radial components of the magnetic field have been disregarded[18], and $f_{st}(\rho,\mu,p)$ has been chosen to be normalized to the suprathermal electron density, $n_{st}(\rho)$, according to

$$\int_0^{2\pi} d\phi \int_{-1}^{+1} d\mu \int_0^{\infty} dp\, p^2\, f_{st}(\rho,\mu,p) = n_{st}(\rho)\,. \tag{5}$$

The symmetry of the problem may be taken advantage of by using the Legendre polynomials[19], $P_n(z)$, and by expanding $d\sigma^{BE}_{e\text{-}i}(h\nu,p,\vec{e_\nu}.\vec{e_p},Z_i)/d\Omega dh\nu$ and $f_{st}(\rho,\mu,p)$ in the series

$$\frac{d\sigma^{BE}_{e\text{-}i}(h\nu,p,\vec{e_\nu}.\vec{e_p},Z_i)}{d\Omega dh\nu} = \sum_{n=0}^{\infty}\left(n+\frac{1}{2}\right)\frac{d\sigma_n(h\nu,p,Z_i)}{d\Omega dh\nu}\,P_n(\vec{e_\nu}.\vec{e_p})\,, \tag{6a}$$

$$\frac{d\sigma_n(h\nu,p,Z_i)}{d\Omega dh\nu} = \int_{-1}^{+1} d(\vec{e_\nu}.\vec{e_p})\,\frac{d\sigma^{BE}_{e\text{-}i}(h\nu,p,\vec{e_\nu}.\vec{e_p},Z_i)}{d\Omega dh\nu}\,P_n(\vec{e_\nu}.\vec{e_p})\,, \tag{6b}$$

$$f_{st}(\rho,\mu,p) = \sum_{n=0}^{\infty}\left(n+\frac{1}{2}\right) f_n(\rho,p)\,P_n(\mu)\,, \tag{7a}$$

$$f_n(\rho,p) = \int_{-1}^{+1} d\mu\, f_{st}(\rho,\mu,p)\,P_n(\mu)\,. \tag{7b}$$

It is then straightforward to rewrite Eq. (4) in the form

$$\frac{dn_{h\nu}(\rho,\varphi)}{d\Omega dt dh\nu} \equiv 2\pi \sum_{i=He,C} n_i(\rho) \sum_{n=0}^{\infty}\left(n+\frac{1}{2}\right) P_n(\cos\varphi)$$

$$\times \int_{p_{min}}^{\infty} dp\,\frac{d\sigma_n(h\nu,p,Z_i)}{d\Omega dh\nu}\,\frac{p^3 c}{\left(p^2+m_e^2c^2\right)^{1/2}}\,f_n(\rho,p)\,, \tag{8}$$

where use has been made of the appropriate addition theorem[19].

As the HXR diagnostic installed in TORE SUPRA has its lines-of-sight lying in a poloidal cross section, the detected emission is perpendicular to the toroidal magnetic field, and so $\varphi = \pi/2$. In this case, Eqs. (1), (2), and (8) put together give[17]

$$\frac{dN_H}{dtdh\nu} \equiv 2\pi \left(\frac{\pi r_1 r_2}{b}\right)^2 \int_0^\infty dh\nu' \lambda_a(h\nu')\left[1 - \lambda_d(h\nu')\right] g_d(h\nu', H) \int_L dl \sum_{i=He,C} n_i(\rho)$$

$$\times \sum_{n=0}^{\infty} \left(n + \frac{1}{2}\right) P_n(0) \int_{p_{min}}^{\infty} dp \frac{d\sigma_n(h\nu', p, Z_i)}{d\Omega dh\nu'} \frac{p^3 c}{(p^2 + m_e^2 c^2)^{1/2}} f_n(\rho, p) \,. \qquad (9)$$

The predicted HXR spectra discussed in this work have been obtained using 40 flux surfaces, 51 Legendre polynomials, 31 points in hν, and 51 points in p. The coefficients $d\sigma_n(h\nu,p,Z_i)/d\Omega dh\nu$ and $f_n(\rho,p)$, defined by Eqs. (6) and (7), have been computed by means of a Gauss-Legendre integration[20] and with 71 points in θ.

D. Radial diffusion of suprathermal electrons

The simulation code deals with radial diffusion of suprathermal electrons by diffusing the LH-driven current density, $J_{LH}(\rho)$, so the diffusion coefficient is an eigenvalue of a boundary value problem consistent with a global conservation law given by the Fokker-Planck equation[3]. Since the radial diffusion calculation is not performed on the electron distribution function itself, but rather on its current density moment, some assumptions have to be made in order to link the diffused LH-driven current density, $J^*_{LH}(\rho)$, with the diffused profile for the suprathermal electron distribution function, $f^*_{st}(\rho,\mu,p)$, if the influence of radial diffusion on the predicted HXR emission is to be assessed.

Numerical studies using a three-dimensional Fokker-Planck analysis have shown[21] that radial diffusion does not significantly distort $f_{st}(\rho,\mu,p)$ in momentum space: the effective perpendicular temperature is not appreciably modified and the shape of the LH-generated plateau is conserved. Indeed, suprathermal electrons are radially redistributed by essentially changing the plateau level on each flux surface. So, it seems reasonable to consider that the $J^*_{LH}(\rho)$ and $f^*_{st}(\rho,\mu,p)$ profiles have roughly the same form[22],

$$f^*_{st}(\rho,\mu,p) \equiv \chi(\mu,p)\, J^*_{LH}(\rho) \,, \qquad (10)$$

and that the suprathermal electron density in momentum space is conserved[23],

$$\int_0^1 d\rho\ \rho\ f^*_{st}(\rho,\mu,p) \equiv \int_0^1 d\rho\ \rho\ f_{st}(\rho,\mu,p)\ . \tag{11}$$

Hence,

$$\chi(\mu,p) \equiv \frac{\displaystyle\int_0^1 d\rho\ \rho\ f_{st}(\rho,\mu,p)}{\displaystyle\int_0^1 d\rho\ \rho\ J^*_{LH}(\rho)}\ . \tag{12}$$

It is understood that Eqs. (10) to (12) may oversimplify some aspects of the radial diffusion process undergone by suprathermal electrons. Nevertheless, they suffice for the purpose of estimating in which way such process may modify the HXR spectra. From Eqs. (7), (10), and (12), it is straightforward to see that the modified HXR spectra can be obtained by replacing, in Eq. (9), $f_n(\rho,p)$ by

$$f^*_n(\rho,p) \equiv J^*_{LH}(\rho)\frac{\displaystyle\int_0^1 d\rho'\ \rho'\ f_n(\rho',p)}{\displaystyle\int_0^1 d\rho'\ \rho'\ J^*_{LH}(\rho')}\ . \tag{13}$$

For the plasma considered here, the radial diffusion calculation for the LH-driven current density has given a diffusion coefficient of about 1 $m^2 sec^{-1}$. Collisional slowing down prevails in the inner half of the discharge ($n_{e0} \approx 5.3 \times 10^{19}$ m^{-3} and $\langle n_e \rangle \approx 3.3 \times 10^{19}$ m^{-3}), so radial diffusion is felt mainly in the outer half. This can be seen in Fig. 2, which shows $J_{LH}(\rho)$ and $J^*_{LH}(\rho)$. Therefore, predicted HXR data for the most peripheral lines-of-sight D and E may be expected to depend on radial diffusion of suprathermal electrons in a non-negligible manner.

E. Radiation scattering by the inner wall

Photons impinging upon the inner wall (1 cm thick graphite tiles brazed on a steel structure) can emerge back at lower energy, after going through a random walk process inside it, in which Compton scattering and absorption by way of the photoelectric effect are the dominant interactions[24]. As a consequence, the contribution of the radiation thus scattered to the HXR emission detected by a line-of-sight intersecting the inner wall can be large as compared to the direct plasma contribution[13]. Obviously, the importance of this effect depends on the level of the plasma HXR emission, as well as on its radial and energy distributions.

For a line-of-sight intersecting the wall at a poloidal location Θ and with an angle Φ with respect to the direction locally perpendicular to the wall surface, the scattered photon spectrum is given by the relation

$$\frac{dN^s_{h\nu}}{dtdh\nu} \cong \left(\frac{\pi r_1 r_2}{b}\right)^2 \frac{dn^s_{h\nu}(\Theta,\Phi)}{d\Omega dtdh\nu}, \tag{14}$$

with $dn^s_{h\nu}(\Theta,\Phi)/d\Omega dtdh\nu$ the surface density of photons at Θ that are scattered off the wall with energy $h\nu$ in the direction Φ, per solid angle $d\Omega$, time interval dt, and energy range $dh\nu$. If the energy and incidence-angle distributions of impinging photons are known, $dn^s_{h\nu}(\Theta,\Phi)/d\Omega dtdh\nu$ can be obtained after solving, inside the inner wall, the transport equation for the radiation. This is accomplished by means of a Monte Carlo calculation in slab geometry, which constitutes a standard approach for treating HXR penetration and diffusion problems[24]. Since the inner wall integrates a photon flux coming from nearly all directions, it is possible to assume that the wall views an isotropic plasma HXR emission. Furthermore, if the "photon temperature" does not vary significantly from one line-of-sight to another, as is to be verified in the present case, the energy dependence of the HXR emission can be considered to be the same throughout the plasma. The "photon temperature", T_{ph}, is a useful parameter to characterize the energy dependence of the HXR spectra[9-12,14], and is defined according to

$$\frac{dN_H}{dtdh\nu} \propto \frac{1}{h\nu} \exp\left(-\frac{h\nu}{T_{ph}}\right). \tag{15}$$

Under these conditions, and for the purpose of computing the energy and incidence-angle distributions of photons coming from the plasma and impinging upon the wall, which are the necessary inputs for the Monte Carlo calculation, $dn_{h\nu}(\rho,\varphi)/d\Omega dtdh\nu$ is approximated by

$$\frac{dn_{h\nu}(\rho,\varphi)}{d\Omega dt dh\nu} \cong \frac{1}{4\pi}\frac{dn_{ph}(\rho)}{dt}\frac{1}{(h\nu_{av} - h\nu_{min})}\exp\left(-\frac{h\nu - h\nu_{min}}{h\nu_{av} - h\nu_{min}}\right), \quad (16)$$

where $dn_{ph}(\rho)/dt$ is the density of photons that are emitted at ρ, per time interval dt, and $h\nu_{min}$ and $h\nu_{av}$ the minimum and average energy values, respectively. The form of Eq. (16) has the advantage of enabling the decorrelation of those two distributions. In particular, the incidence-angle distribution is derived by an appropriate volume and solid-angle integration of $dn_{ph}(\rho)/dt$ over all plasma cells that contribute to the radiation entering the inner wall at its intersection surface with the line-of-sight. Such integration takes into account the tokamak toroidal geometry.

For the diagnostic set-up of Fig. 1, the contribution of the scattered photon spectrum to the predicted HXR data has to be assessed only for lines-of-sight D and E, since lines-of-sight A, B, and C face the upper port, which acts as a radiation dump. For TORE SUPRA shot #5319, the values $h\nu_{min} = 20$ keV and $h\nu_{av} = 70$ keV have been used. Following a logical procedure, the corrections due to radiation scattering by the inner wall have been obtained after radially diffusing the suprathermal electrons.

F. Measurement of the HXR spectra

Measured HXR spectra are recorded using a standard multi-channel analyzer, which is composed of a charge pre-amplifier, a pulse shaping amplifier, an analog-digital convertor, and a histogramming memory unit. The measuring system is not prepared to automatically correct for pile-up and dead-time errors. In order to reduce these, the pulse rise time is set to 0.587 μsec, for a total pulse duration not exceeding 1.825 μsec. The time it takes to digitalize and memorize the pulse, 3.0 μsec, is independent of the pulse height and larger than the pulse duration, so practically no distortion is introduced in the energy dependence of the measured spectra. However, dead-time effects have to be seriously considered at high counting rate, since the actual number of recorded counts, N_H^I, can be significantly lower than the number of input pulses, N_H.

Therefore, the measured spectra have been corrected by way of a Monte Carlo calculation that simulates both pile-up and dead-time effects. For the conditions corresponding to TORE

SUPRA shot #5319, the relation between N_H^r and N_H is plotted in Fig. 3. In this way, and if it is assumed that N_H is always lower than 500 kHz, which is confirmed experimentally by the absence of saturation effects in the charge pre-amplifier, N_H can be recovered once N_H^r is known. The experimental error in N_H is mainly due to the statistical dispersion of the pulse-counting process, and is $\pm (N_H)^{1/2}$. An acquisition time of 0.5 sec and energy intervals of 4 keV have been used in recording the HXR spectra discussed below.

III. RESULTS AND DISCUSSION

The measured and predicted HXR spectra for TORE SUPRA shot #5319 are depicted in Fig. 4. Before applying the LH power, low-level signals are detected up to $h\nu \approx 50$ keV. Once the LH pulse is on, a large increase in the counting rate is observed and the HXR spectra extend up to $h\nu \approx 400$ keV. For all lines-of-sight, the measured HXR spectrum decreases rapidly when the photon energy increases, and a significant spread of the experimental data occurs for $h\nu \geq 250$ keV. This data spread takes place within the statistical dispersion represented by the error bars, indicating that the signals have dropped to the noise level. It must be noted that, even without taking into account radial diffusion of suprathermal electrons and radiation scattering by the inner wall, both the energy dependence and the magnitude of the measured HXR spectra are fairly well reproduced in the range $30 \text{ keV} \leq h\nu \leq 250$ keV, except for line-of-sight E.

Corrections due to radial diffusion of suprathermal electrons are important, in the present case, only for lines-of-sight D and E, in particular for the last one. This can be understood with the help of Fig. 2 and by considering that, as can be seen in Fig. 1, those two lines-of-sight probe the outer half of the plasma, which is the region most affected by the diffusion process. The effect of radiation scattering by the inner wall is negligible (less than 2%) for line-of-sight D and significant (about 40%) for line-of-sight E.

The measured and predicted values of T_{ph} for the different lines-of-sight, calculated in the interval $75 \text{ keV} \leq h\nu \leq 225$ keV, are given in Fig. 5 and compare well with each other.

Moreover, the fact that T_{ph} is practically the same for all lines-of-sight validates the assumption made in writing Eq. (16), according to which the radial variation in the energy dependence of the HXR emission is weak.

Notwithstanding some discrepancies that remain to be explained, a fair agreement exists between the measured and predicted HXR data. It is worth emphasizing that the latter have been derived from an electron distribution function coming out from a calculation that has also reproduced, within an acceptable uncertainty, the other experimental signals[4]. The overall underestimation of the HXR emission may result from having computed the effective perpendicular temperature in the nonrelativistic limit, which gives a lower value for it[15], and also from having disregarded the contribution to Z_{eff} of heavy impurities, such as iron. For line-of-sight E, it may also be invoked the fact that Z_{eff} has been assumed to be constant throughout the plasma cross section, although a pronounced increase in its value is likely to occur close to the plasma edge. A detailed assessment of these effects is somewhat futile here, since there is available no more quantitative experimental information regarding them than the one that has been incorporated in the computations. So, it is always possible to find some reasonable models for the concentration of heavy impurities and for the Z_{eff} profile such that the measured HXR spectra can be better fitted. However, that is not the purpose of the present work. To be retained is the fact that a simulation based on self-consistent ray-tracing and Fokker-Planck calculations of the LH wave propagation and absorption and of the electron dynamics has succeeded in modeling a typical LH current drive experiment, in a way that is consistent with a broad set of experimental data.

IV. SUMMARY AND CONCLUSIONS

A detailed analysis has been presented demonstrating the ability of combined ray-tracing and Fokker-Planck calculations to predict the HXR emission during LH current drive in tokamaks when toroidally induced ray stochasticity is important. Furthermore, it has been shown that both radial diffusion of suprathermal electrons and radiation scattering by the inner

wall play, in general, a non-negligible role in explaining the experimentally observed features of the HXR emission.

This work confirms previous results[4,5] according to which ray tracing is indeed capable of describing, in a Monte Carlo-like manner, the LH wave propagation and absorption when the ray dynamics is stochastic, provided a sufficiently large number of rays is used. It may thus be concluded that combined ray-tracing and Fokker-Planck codes do contain the basic ingredients to correctly model the physics of LH current drive in tokamaks. Obviously, a number of improvements can still be introduced in order to obtain a finer fitting between measurements and predictions.

ACKNOWLEDGMENTS

The authors wish to thank Dr. Christian Janicki for useful comments on the manuscript.

The present paper is part of the work carried out by the first author (J. P. B.) in fulfilment of the requirements for obtaining the Doctorate degree (Université de Provence, Aix-Marseille I). The same author acknowledges support by the Commission of the European Communities under Euratom Grant No. B 89000563.

REFERENCES

[a]Permanent address: Centro de Fusão Nuclear, Associação Euratom-IST, Instituto Superior Técnico, 1096 Lisboa Codex, Portugal.

[b]Plasma Fusion Center, Massachusetts Institute of Technology, Cambridge, Massachusetts 02139.

[c]Centre Canadien de Fusion Magnétique, Varennes, Québec J3X 1S1, Canada.

[d]MPB Technologies Inc., Pointe claire, Québec H9R 1E9, Canada.

[1]P. T. Bonoli and R. C. Englade, Phys. Fluids **29**, 2937 (1986).

[2]P. T. Bonoli, M. Porkolab, Y. Takase, and S. F. Knowiton, Nucl. Fusion **28**, 991 (1988).

[3]V. Fuchs, I. P. Shkarofsky, R. A. Cairns, and P. T. Bonoli, Nucl. Fusion **29**, 1479 (1989).

[4]J. P. Bizarro and D. Moreau, Phys. Fluids B **5**, No. 4 (1993).

[5]J. P. Bizarro, Nucl. Fusion **33**, in press (1993).

[6]J.-M. Wersinger, E. Ott, and J. M. Finn, Phys. Fluids **21**, 2263 (1978).

[7]P. T. Bonoli and E. Ott, Phys. Fluids **25**, 359 (1982).

[8]S. von Goeler, J. Stevens, S. Bernabei, M. Bitter, T. K. Chu, P. Efthimion, N. Fisch, W. Hooke, K. Hill, J. Hosea, F. Jobes, C. Karney, J. Mervine, E. Meservey, R. Motley, P. Roney, S. Sesnic, K. Silber, and G. Taylor, Nucl. Fusion **25**, 1515 (1985).

[9]J. Stevens, S. von Goeler, S. Bernabei, M. Bitter, T. K. Chu, P. Efthimion, N. Fisch, W. Hooke, J. Hosea, F. Jobes, C. Karney, E. Meservey, R. Motley, and G. Taylor, Nucl. Fusion **25**, 1529 (1985).

[10]S. von Goeler, J. Stevens, S. Bernabei, M. Bitter, T. K. Chu, F. Jobes, K. Hill, W. Hooke, J. C. Hosea, H. Hsuan, E. Mazzucato, E. Meservey, R. W. Motley, and S. Sesnic, Rev. Sci. Instrum. **57**, 2130 (1986).

[11]S Texter, S. Knowlton, M. Porkolab, and Y. Takase, Nucl. Fusion **26**, 1279 (1986).

[12]K. Ogura, H. Tanaka, S. Ide, M. Iida, K. Hanada, M. Yoshida, T. Minami, T. Cho, M. Nakamura, T. Maekawa, Y. Terumichi, and S. Tanaka, Nucl. Fusion **31**, 1015 (1991).

[13]Y. Peysson, J. P. Bizarro, G. T. Hoang, A. Hubbard, X. Litaudon, D. Moreau, C. Poitou-Pocheau, and J. M. Rax, in *Proceedings of the 18th European Conference on Controlled*

Fusion and Plasma Physics, Berlin, edited by P. Bachmann and D. C. Robinson (European Physical Society, Geneva, Switzerland, 1991), Vol. 15 C, Part IV, p. 345.

[14]Y. Peysson, P. Froissard, J. P. Bizarro, M. Brusati, J. Carrasco, A. Ekedahl, C. Gormezano, G. T. Hoang, J. Jacquinot, K. Kupfer, X. Litaudon, D. Moreau, D. Pasini, J. M. Rax, D. Rigaud, and F. Rimini, in *Proceedings of the Europhysics Topical Conference on Radiofrequency Heating and Current Drive of Fusion Devices*, Brussels, edited by C. Gormezano, P. U. Lamalle, and R. R. Weynants (European Physical Society, Geneva, Switzerland, 1992), Vol. 16 E, p. 217.

[15]I. P. Shkarofsky, V. Fuchs, M. Shoucri, P. Bonoli, A. Bers, R. A. Cairns, and C. N. Lashmore-Davies, in *Proceedings of the 9th Topical Conference on Radio-Frequency Power in Plasmas*, Charleston, edited by D. B. Batchelor (American Institute of Physics, New York, 1992), No. 244, p. 280.

[16]D. A. Ehst and C. F. F. Karney, Nucl. Fusion **31**, 1933 (1991).

[17]It is clear that, whenever a line-of-sight integral appears in the text, ρ and φ are to be taken locally along the line-of-sight.

[18]Actually, the suprathermal electron distribution function is $f_{st}(\rho,\mu',p)$, where $\mu' = (\vec{e}_p.\vec{B})/|\vec{B}|$, with $\vec{B}$ the total magnetic field. Let $\vec{B}_t$, $\vec{B}_p$, and $\vec{B}_r$ denote the toroidal, poloidal, and radial components of $\vec{B}$, respectively. Then,

$$\mu' = \frac{B_t}{|\vec{B}|}\mu + \frac{(\vec{B}_p + \vec{B}_r)}{|\vec{B}|}.\vec{e}_p .$$

[19]I. S. Gradshteyn and I. M. Ryzhik, *Table of Integrals, Series, and Products* (Academic Press, New York, 1965).

[20]W. H. Press, B. P. Flannery, S. A. Teukolsky, and W. T. Vetterling, *Numerical Recipes* (Cambridge University Press, Cambridge, 1986).

[21]G. Giruzzi, Plasma Phys. Controlled Fusion **35**, A123 (1993).

[22]The relation given by Eq. (10) can be derived by representing $f^*_{st}(\rho,\mu,p)$ in terms of a plateau in parallel momentum and a Maxwellian distribution in perpendicular momentum such that the

effective perpendicular temperature, $T_\perp$, and the plateau limits, $p_{//min}$ and $p_{//max}$, have a weak dependence on ρ in the region where the level of $J^*_{LH}(\rho)$ is significant. Then,

$$f^*_{st}(\rho,\mu,p) \cong \frac{H(p_{//max} - \mu p)\, H(\mu p - p_{//min})}{2\pi m_e T_\perp} \frac{n_{st}(\rho)}{(p_{//max} - p_{//min})} \exp\left[-\frac{(1-\mu^2)p^2}{2m_e T_\perp}\right],$$

with $H(z)$ the Heaviside function, and it is straightforward, although lengthy, to show that

$$\chi(\mu,p) \cong \frac{H(p_{//max} - \mu p)\, H(\mu p - p_{//min})}{\pi e (2m_e T_\perp)^{3/2}}$$

$$\times \left[\Psi\left(-\frac{1}{2}, -\frac{1}{2}, \frac{m_e^2c^2 + p^2_{//max}}{2m_e T_\perp}\right) - \Psi\left(-\frac{1}{2}, -\frac{1}{2}, \frac{m_e^2c^2 + p^2_{//min}}{2m_e T_\perp}\right)\right]^{-1} \exp\left[-\frac{(1-\mu^2)p^2}{2m_e T_\perp}\right].$$

Here, e is the electron charge, $\Psi(1-\alpha, 1-\alpha; z) = \Gamma(\alpha,z)\exp(z)$ a degenerate hypergeometric function, and $\Gamma(\alpha,z)$ an incomplete gamma function[19]. In the limit $m_e^2c^2 \gg p^2_{//max} > p^2_{//min} \gg 2m_eT_\perp$,

$$\chi(\mu,p) \cong \frac{H(p_{//max} - \mu p)\, H(\mu p - p_{//min})}{\pi e T_\perp} \frac{1}{(p^2_{//max} - p^2_{//min})} \exp\left[-\frac{(1-\mu^2)p^2}{2m_e T_\perp}\right].$$

[23]It is immediate to check that Eq. (11) is consistent with the conservation of the LH-driven current,

$$\int_0^1 d\rho\, \rho\, J^*_{LH}(\rho) \cong \int_0^1 d\rho\, \rho\, J_{LH}(\rho),$$

the latter being assumed when diffusing the LH-driven current density[3].

[24]U. Fano, L. V. Spencer, and M. J. Berger, in *Encyclopedia of Physics*, edited by S. Flügge (Springer-Verlag, Berlin, 1959), Vol. XXXVIII/2, p. 660.

FIGURE CAPTIONS

FIG. 1. Schematic of the HXR diagnostic installed in TORE SUPRA.

FIG. 2. Predicted nondiffused and diffused LH-driven current density profiles.

FIG. 3. Computed relation between the number of input pulses and the number of recorded counts. The dashed line corresponds to $N_H^r = N_H$.

FIG. 4. Measured and predicted HXR spectra. (a) Line-of-sight A. (b) Line-of-sight B. (c) Line-of-sight C. (d) Line-of-sight D. (e) Line-of-sight E. The black (white) squares correspond to the measured HXR spectra in the Ohmic-LH (Ohmic) steady state. Dashed lines (crosses) correspond to the predicted HXR spectra without (with) corrections due to radial diffusion of suprathermal electrons. In Fig.4 (e), the dotted line corresponds to the predicted spectrum scattered by the inner wall and the dot-dashed line to the predicted HXR spectrum with corrections due to radial diffusion of suprathermal electrons and to radiation scattering by the inner wall.

FIG. 5. Measured and predicted "photon temperatures".

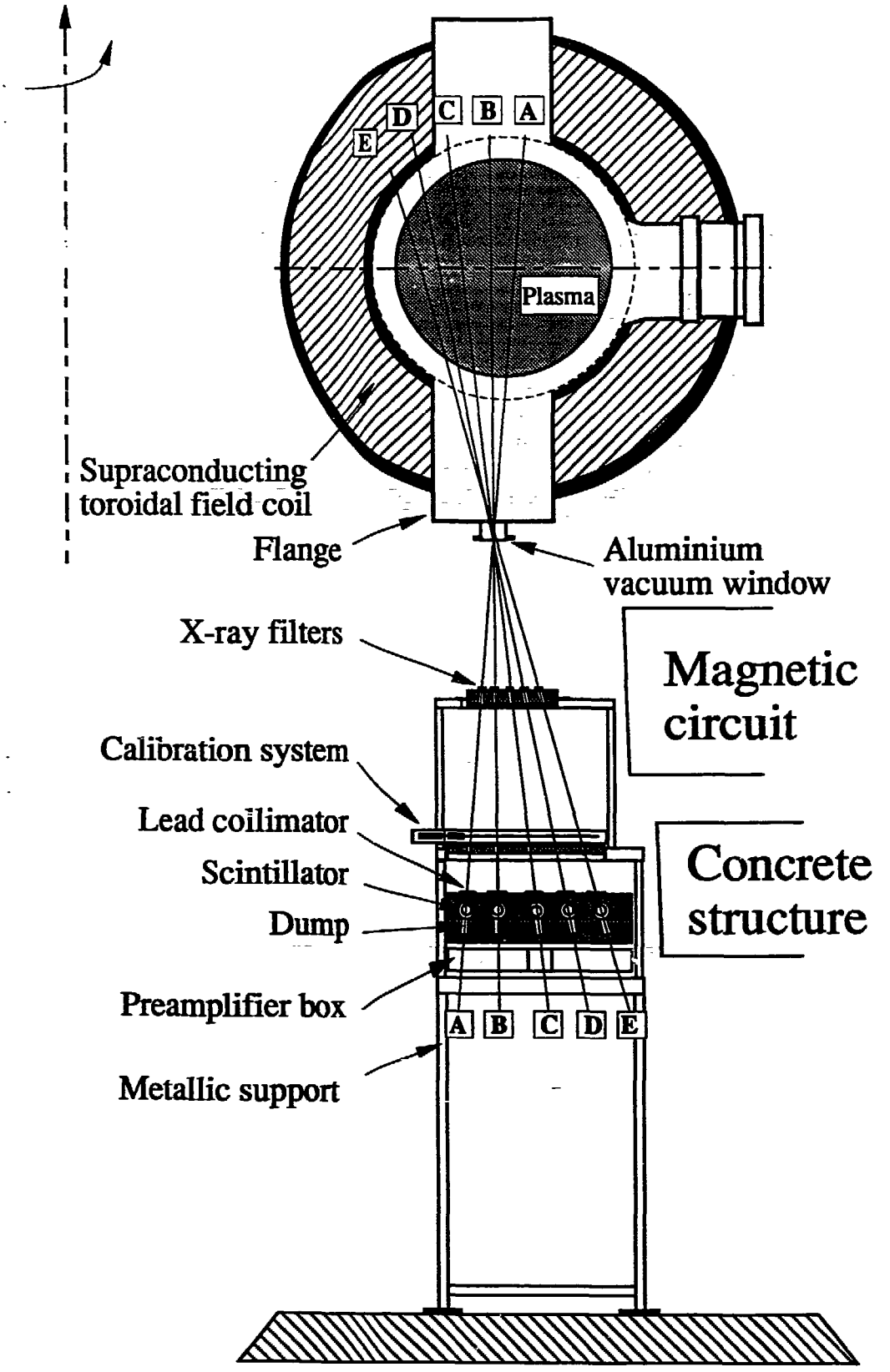
D
C
B
A
E
Plasma
Supraconducting toroidal field coil
Flange
Aluminium vacuum window
X-ray filters
Magnetic circuit
Calibration system
Lead collimator
Scintillator
Dump
Concrete structure
Preamplifier box
A
B
C
D
E
Metallic support

Figure 1

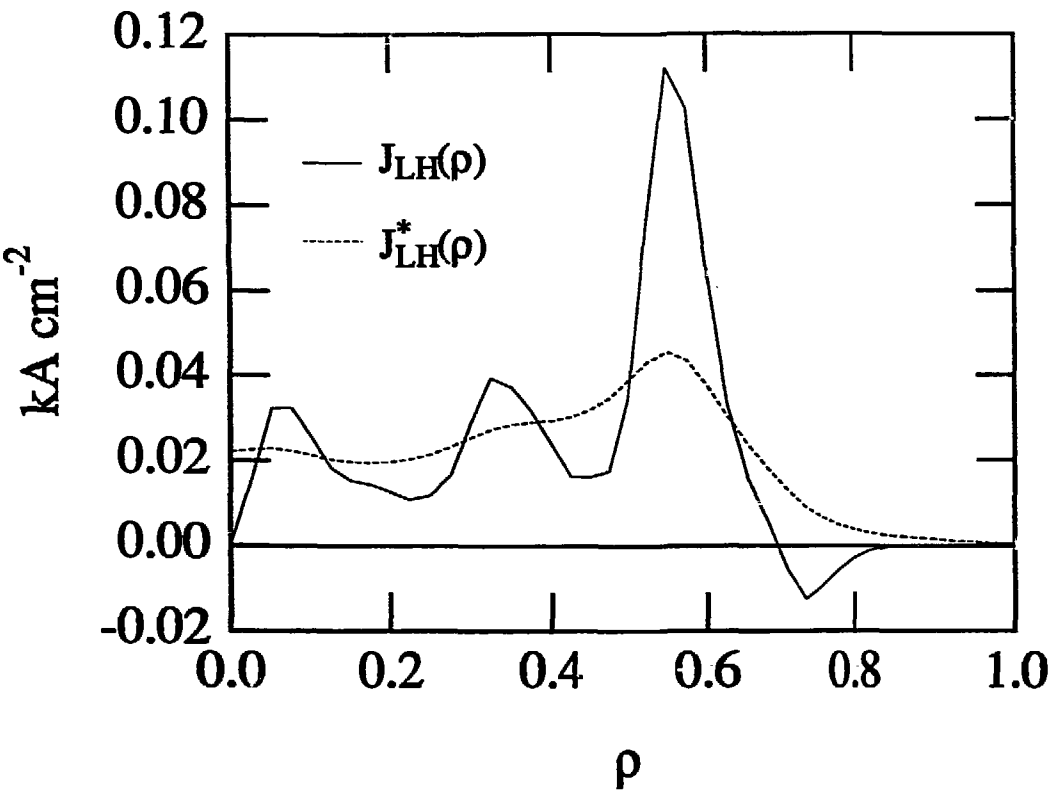
0.12
0.10
0.08
0.06
0.04
0.02
0.00
-0.02
kA cm-2
JLH(ρ)
J*LH(ρ)
0.0
0.2
0.4
0.6
0.8
1.0
ρ

Figure 2

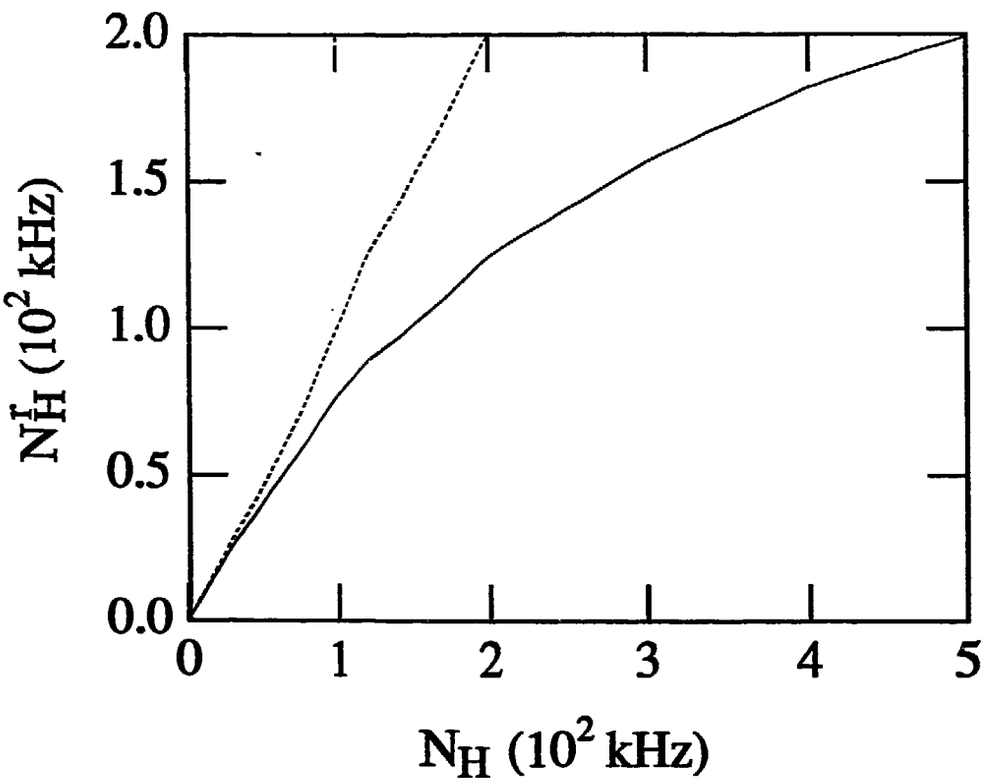

Figure 3

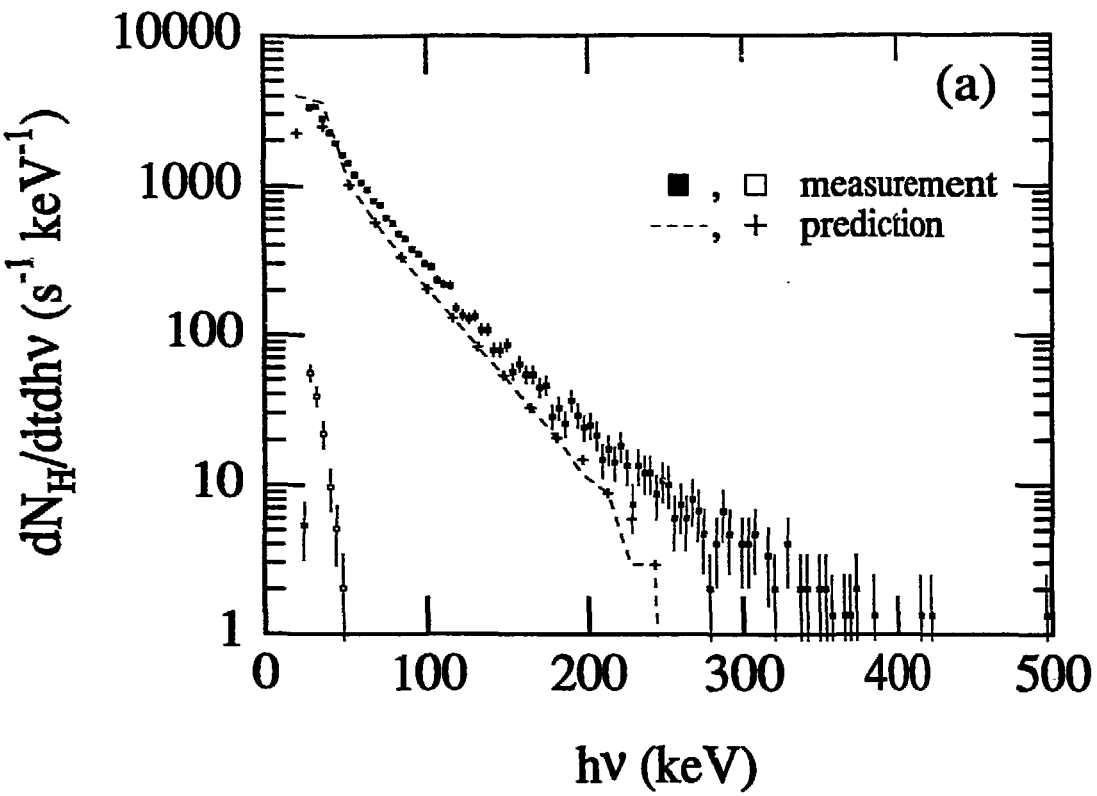
10000
1000
100
10
1
0
100
200
300
400
500
(a)
■ , □ measurement
----, + prediction
dN_H/dtdhν (s^-1 keV^-1)
hν (keV)

Figure 4(a)

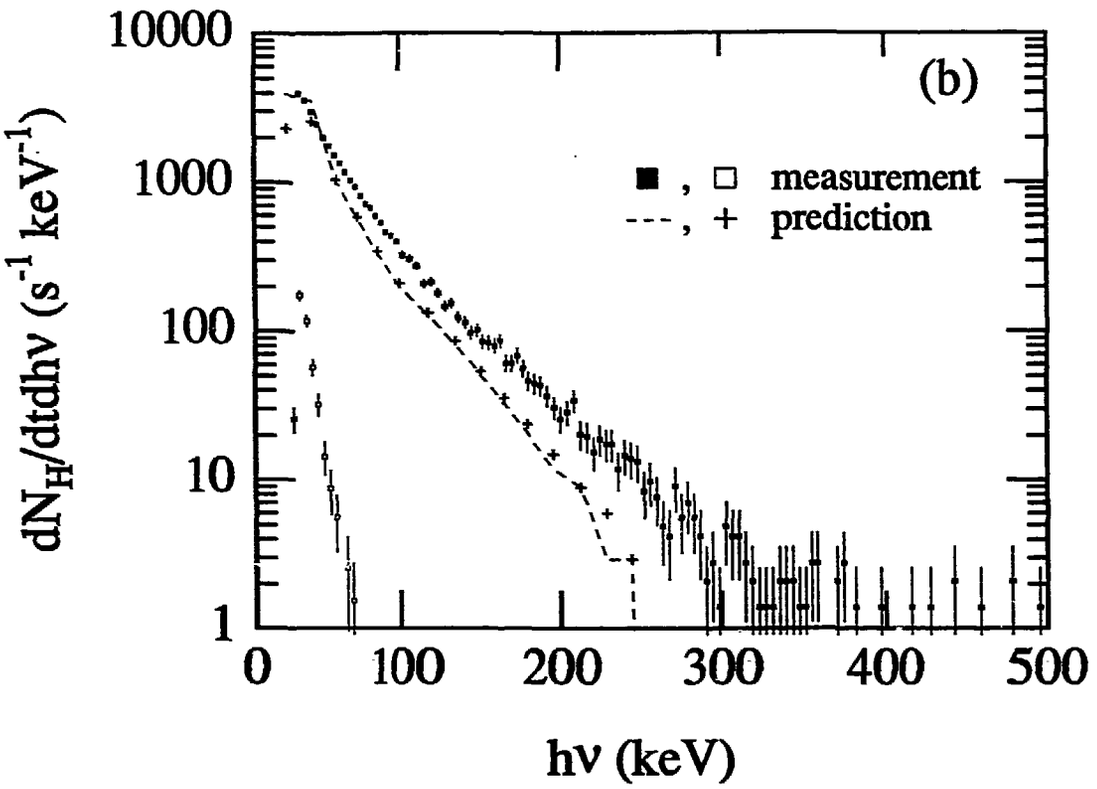
10000
1000
100
10
1
0
100
200
300
400
500
(b)
■ , □ measurement
---, + prediction
dN_H/dtdhν (s^-1 keV^-1)
hν (keV)

Figure 4(b)

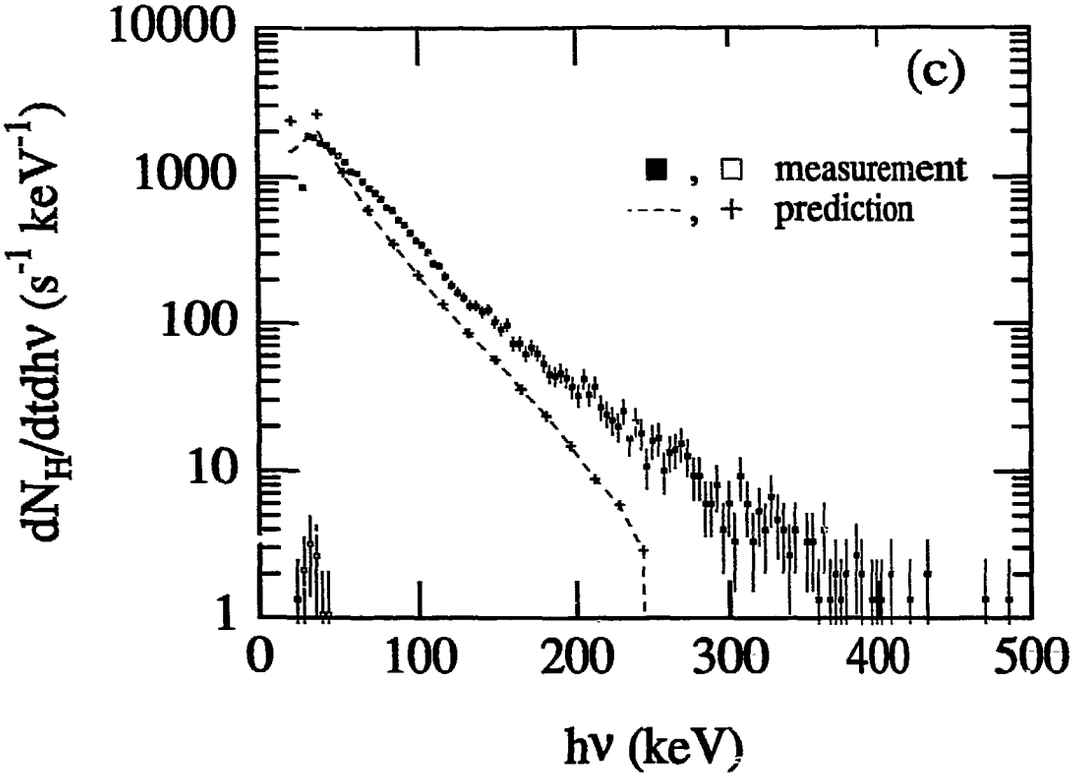
10000
1000
100
10
1
0
100
200
300
400
500
(c)
■ , □ measurement
----, + prediction
dN_H/dtdhν (s^-1 keV^-1)
hν (keV)

Figure 4(c)

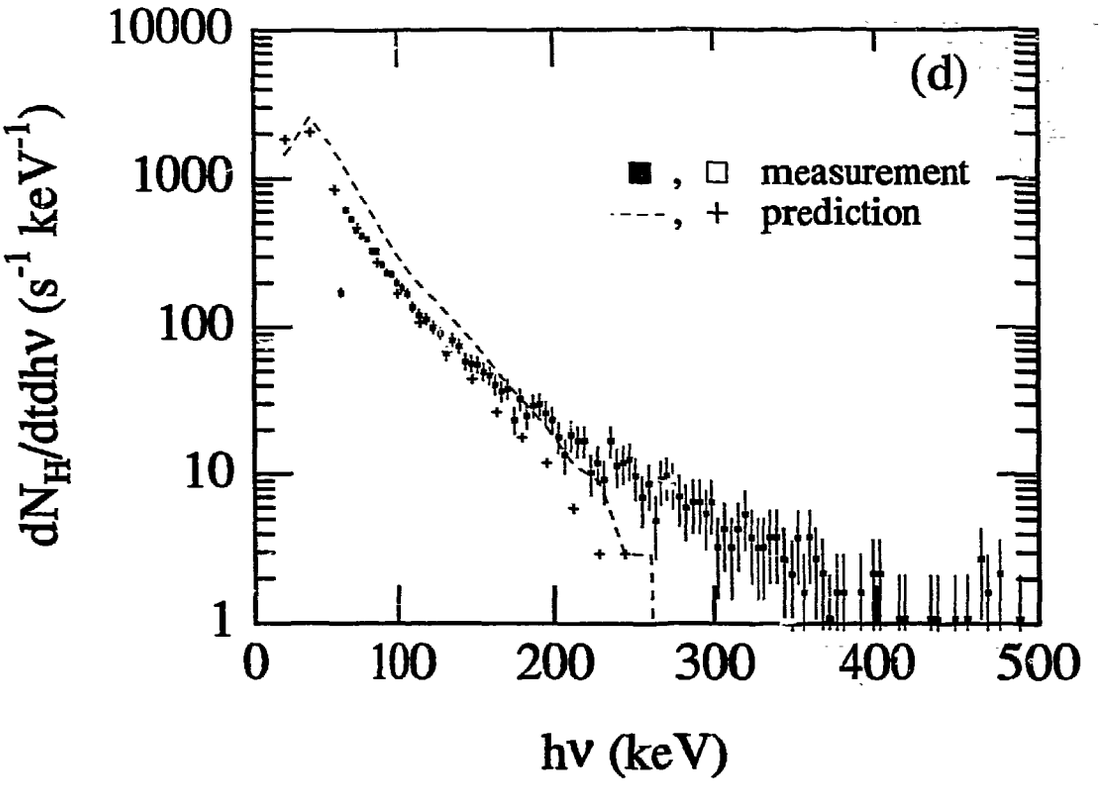
10000
1000
100
10
1
0
100
200
300
400
500
(d)
■ , □ measurement
----, + prediction
dN_H/dtdhν (s^-1 keV^-1)
hν (keV)

Figure 4(d)

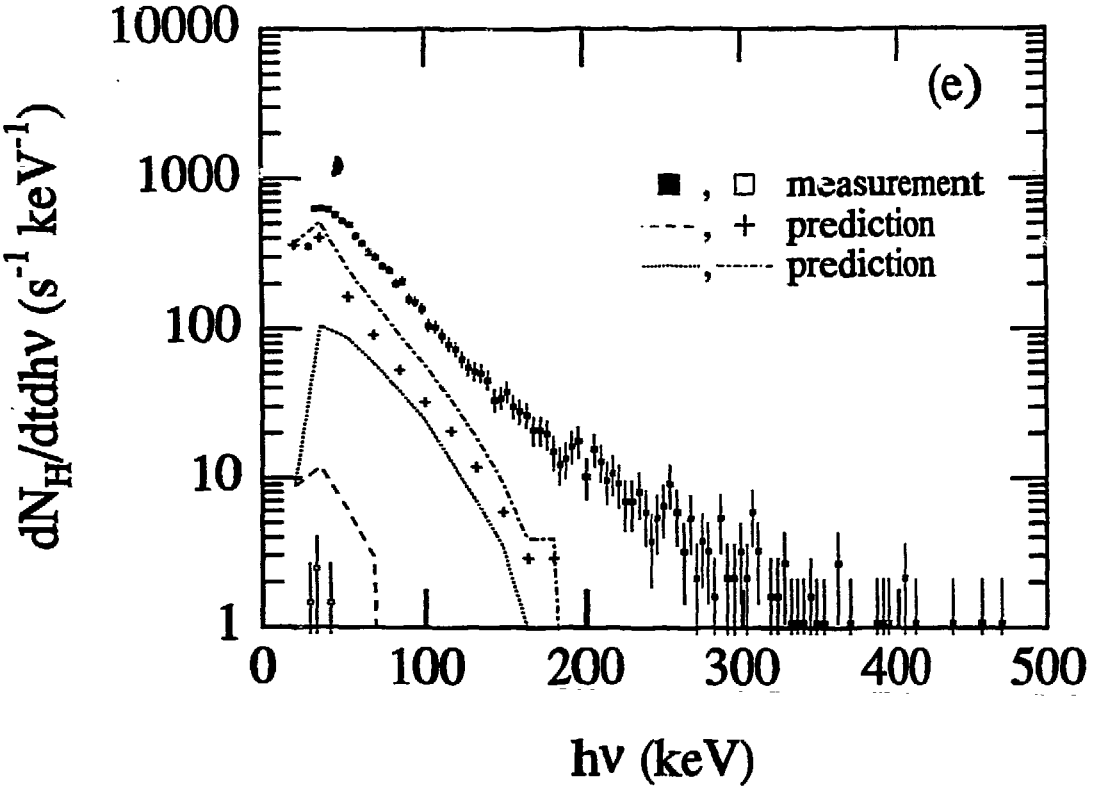
10000
1000
100
10
1
0
100
200
300
400
500
(e)
■ , □ measurement
----, + prediction
——,------ prediction
$dN_H/dtdh\nu$ (s^{-1} keV^{-1})
hν (keV)

Figure 4(e)

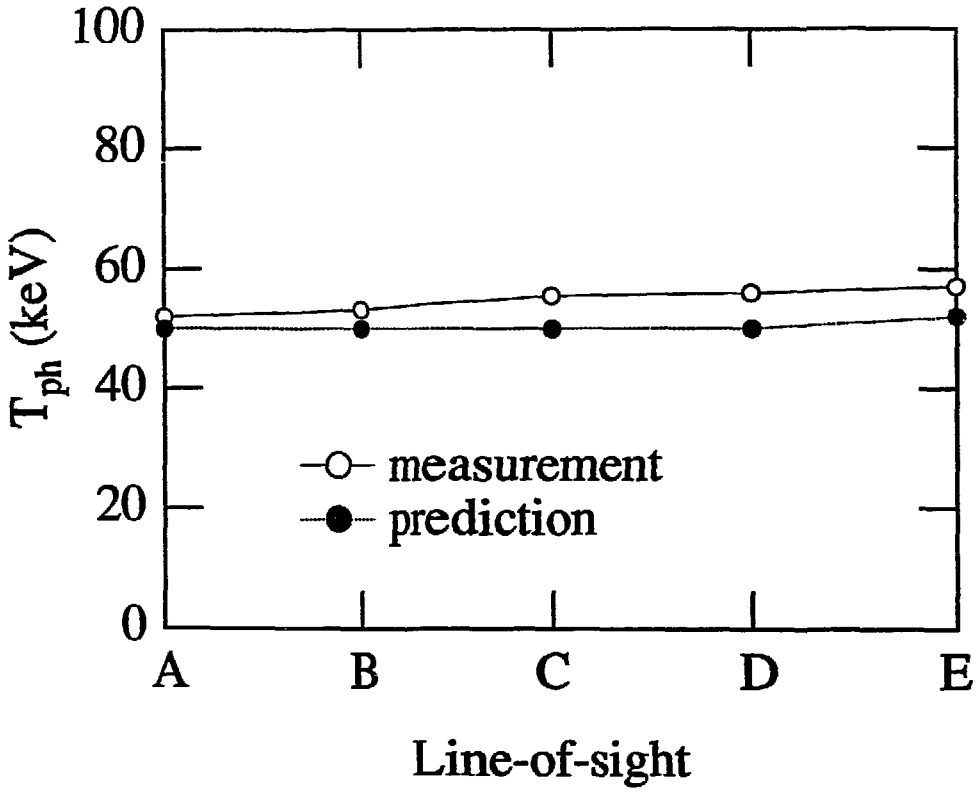
100
80
60
40
20
0
T_{ph} (keV)
measurement
prediction
A
B
C
D
E
Line-of-sight

Figure 5